

# Self-adapting J-type air-based battery thermal management system via model predictive control



Yuanzhi Liu, Jie Zhang\*

The University of Texas at Dallas, Richardson, TX 75080, USA

## HIGHLIGHTS

- A dynamic J-type battery thermal control system is established.
- The mode switching control succeeds to maintain the battery thermal performance.
- The energy efficiency is improved by 15.8% by employing model predictive control.

## ARTICLE INFO

### Keywords:

Battery thermal management system  
Surrogate-based optimization  
J-type structure  
Model predictive control  
Electric vehicles

## ABSTRACT

Battery thermal control plays an indispensable role in terms of the safety and performance for electric vehicles. For air-based cooling technologies, one of the most pressing challenges is to balance the temperature uniformity and constrain the maximum temperature simultaneously under varying driving conditions. This paper proposes a self-adaptive intelligent neural network-based model predictive control strategy for a J-type air-based battery thermal management system. The J-type structure is first optimized through surrogate-based optimization to improve the temperature uniformity before control. Based on the optimized J-type configuration, an operation mode switching module is developed to mitigate the temperature unbalance. The thermal control approach is tested using an integrated driving cycle, and its evaluations are threefold: (i) the neural network-based control without mode switching fails to meet the thermal requirements; (ii) the control with mode switching succeeds in constraining the maximum temperature and maintaining the temperature uniformity within 1.33 K; (iii) the added model predictive control approach slightly enhances the thermal performance but improves the energy efficiency significantly by 15.8%. The results show that the J-type structure with its appropriate control strategy is a promising solution for light-duty electric vehicles using an air-cooling technology.

## 1. Introduction

Lithium batteries, as the primary traction power source, have been extensively employed in electric vehicles (EVs) due to its distinguished properties like high energy density, long cycle life, low self-discharging, and low maintenance [1]. However, several critical issues such as battery cell unbalancing, gradual aging effects, and narrow operating temperature range, still need to be addressed before EVs' next massive expansion [2]. For primary lithium battery technologies nowadays, studies have suggested that the appropriate operating temperature should be maintained between 15 °C to 45 °C due to its intrinsic chemistry and thermal properties [3]. Otherwise, it may trigger capacity reduction, electrode degradation, or even potential safety issues under extreme conditions [4]. Therefore, it is critically important to design and optimally control a battery thermal management system

(BTMS) with high efficiency.

A significant amount of research has been carried out to examine and explore a wide range of heat transfer medium coupled with its appropriate structure. State-of-the-art heat transfer mediums include air, fluid, phase change material, heat pipe, and a hybrid integration of them [5]. All the mediums other than air and fluid are still under laboratory experimental stages due to their complexities and instability. Air-based BTMS is currently widely applied in light-duty EVs due to its unparalleled advantages like light weight, simple structure, and low cost. Although fluid-based cooling technologies are more preferred to address the newly-rising challenges like fast charging, air-based cooling technologies are still worth to be explored especially together with optimal control strategies due to its excellent performance. For instance, Nissan Leaf 2018 and Volkswagen E-Golf 2017 directly utilize a passive air cooling technology, while Renault Zoe40 2017, Chevrolet

\* Corresponding author.

E-mail address: [jiezhang@utdallas.edu](mailto:jiezhang@utdallas.edu) (J. Zhang).

Bolt EV, and Toyota Prius Prime employ an active air cooling strategy. All these vehicle models have been successfully updated for several generations, proving that the air-based system is trustworthy and able to meet the market expectations [6].

One of the most pressing challenges for BTMS is to constrain the temperature within an acceptable range and maintain the temperature uniformity at its package level simultaneously and effectively. Two types of approaches to develop more advanced air-based BTMS regarding the structural redesign and control strategy have been studied extensively in the literature. For structure design and optimization, the commonly-used parallel-channel BTMS configuration is usually referred to as a *U*-type (reverse flow) or a *Z*-type (parallel flow) structure, depending on the air flow direction [7]. Based on the basic structures, several structural modifications have been proposed via optimization or introducing auxiliary components [8], e.g., uneven battery channel interspacing size [9], tapered manifold configurations [10], series cooling structure with reciprocating unit [11], series-parallel mixed cooling configuration [12], parallel structure with jet inlet and multiple vortex generators [13], parallel ventilation with different fan locations for cylindrical battery [14], straight-forward configuration with mist generator [15], and other specific structures that seek to allocate the mass flow rate of each channel uniformly [16]. However, the majority of these studies only optimized the geometry size or structure for a single balanced steady state without any modification and control. The dynamic thermal performances have also rarely been tested or verified under dynamic operating conditions. As a result, when the battery condition changes, i.e., under a dynamic driving condition, a fast charging schedule, or seasonal and regional temperature variations, BTMS may fail to work as effectively as its original optimal design or even lead to critical issues like severe temperature imbalance and potential safety concerns. Moreover, the aforementioned complex structures, as well as the side effects that brought upon themselves, e.g., noise and vibration, are challenging to be generalized and applied in practice.

Developing an appropriate control strategy for the existing air-based BTMS structure is another effective way to achieve the goal of maintaining the operation temperature and uniformity. Several studies have been proposed to integrate appropriate control strategies with the current air-based BTMS at the system level. For instance, Gao et al. [17] developed a fuzzy logic control unit for a straight-forward air-based cooling system, and results showed that the battery temperature was controlled effectively within an appropriate temperature range. Mansouri et al. [18] extended the study of parallel cooling using the model predictive control (MPC) algorithm, and results showed an improvement compared to Toyota Prius baseline performance. He et al. [19] proposed to use a hysteresis control method to exploit the air-based reciprocating cooling so as to achieve optimal cooling effectiveness, which resulted in a desirable 84% reduction in parasitic power consumption. Tao et al. [20] used MPC to regulate the refrigerant compressor and cooling air flow rate to keep an ideal cooling temperature for a hybrid cooling system, and found that both the temperature uniformity and energy efficiency could be improved significantly. Vatanparvar et al. [21] developed a thermal and energy management methodology that optimized the utilization of battery and ultra-capacitor, and the control results showed significant improvements regarding both the thermal performance and energy consumption. It can be summarized that the air flow rate is treated as one of the major state variables in an air-cooling thermal control system for most cases, though the system inputs may differ. Through a frequency or voltage modulation control of the cooling fan or compressor, the air flow rate can be adaptively adjusted according to dynamic battery operating conditions. However, owing to the intrinsic limitations of conventional *U*-type, *Z*-type, or other through-type structures, controlling the air flow rate has a significant impact on temperature rise, but makes little difference regarding the temperature uniformity, especially under large flow rate conditions. Overall, by implementing system control on a

fixed cooling structure, the battery thermal performance has been significantly improved for dynamic cases but probably far from optimum.

To mitigate the gap between structural design and its corresponding control strategy, a novel control-friendly *J*-type air-based BTMS has been proposed in our previous study [22]. By integrating the advantages of conventional *U*- and *Z*-type structures, the *J*-type structure is distinguished by threefold: (i) there are two outlets in the *J*-type structure compared to one outlet in the *U*- and *Z*-type structure; (ii) the flexibility of the controllability have been significantly enhanced by employing two control valves to adjust the opening degree of each outlet simultaneously according to varying driving conditions; (iii) three control modes are predefined for simplification and the temperature uniformity can be enhanced by switching between different working modes, namely, *U*-, *Z*-, and *J*-mode. This paper serves to extend the control strategy for the *J*-type BTMS conjointly and seeks to develop an adaptive control approach for the air-based cooling system via the model predictive control (MPC) strategy. It is worthy mentioning that prior to any control implementations, the channels of the *J*-type structure need to be pre-optimized by using a surrogate-based optimization algorithm, for the reason that the *J*-type optimal configuration is able to uniformize the temperature distribution within a narrow range and lengthen the operation time in *J*-mode with a higher efficiency.

The remainder of the paper is organized as follows. First, a battery system electro-thermal-fluid model is developed in Section 2. Then, based on the optimized structure of the battery system, major modules of the battery thermal control framework are constructed separately in Section 3. The established control systems with varying control algorithms (without operation mode switching, basic neural network-based control, MPC) are tested and analyzed based on an integrated dynamic driving cycle in Section 4. Concluding remarks and future work are discussed in the last section.

## 2. Battery system electro-thermal-fluid modeling

### 2.1. Battery electro-thermal model

Studies have demonstrated that the electro-thermal characteristics of lithium battery are strongly affected by the charging/discharging current, operating temperature, state of charge (SoC) [23]. The simplified first-order lumped equivalent circuit model is adopted to represent the electric relationship of a lithium battery, as shown in Fig. 1.

The electric model consists of an ideal voltage source ( $V_{oc}$ ), an internal resistance ( $R_o$ ), and a parallel RC circuit ( $R_D$ ,  $C_D$ ). The dynamic characteristic of the equivalent circuit is described as:

$$V_t = V_{oc} - IR_D - IR_o + (IR_D)e^{-\frac{t-t_0}{\tau}} \quad (1)$$

where  $V_{oc}$  and  $I$  denote the open circuit voltage and current, respectively, and  $\tau = R_D C_D$  is defined as the time constant. The equivalent heat generated by the resistances  $R_o$  and  $R_D$  is considered equal to the battery internal heat source, as given by:

$$\dot{Q} = I^2 R_D + I^2 R_o \quad (2)$$

where  $\dot{Q}$  represents the battery heat generation rate.

Yang et al. [24,25] have detailed the experimental measurement of these electric parameters using a hybrid pulse power characterization (HPPC) test. Based on the experimental data, the Kriging algorithm is

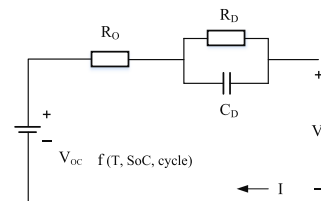
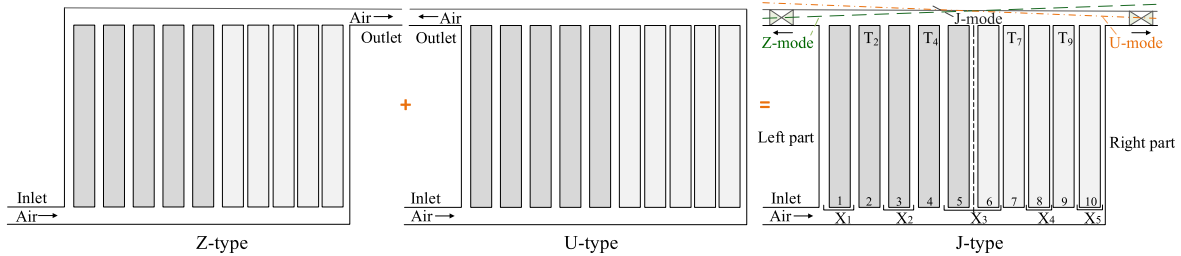


Fig. 1. First-order equivalent circuit model for a lithium battery.



**Fig. 2.** The *J*-type BTMS structure and its control modes.

employed to establish the deterministic electro-thermal estimations, which is formulated as follows.

$$\dot{G}(I, SoC, T) = \dot{Q}(I, SoC, T)/V \quad (3)$$

where denotes the volumetric heat generation rate, and  $V$  is the battery volume. The Kriging algorithm, reasoning process, brief analyses, and model visualization are presented in our previous study [26]. The thermal model is a highly nonlinear and parameter-varying estimation, in which the SoC is generally defined using the Coulomb counting [27], as given by:

$$SoC = SoC_{int} - \frac{\int I dt}{Q_c} \quad (4)$$

where  $SoC_{int}$  and  $Q_c$  denote the SoC at the initial stage and the battery capacity, respectively.  $I$  is the battery current, which is positive for discharging and negative for charging.

## 2.2. Electric and thermal hysteresis analysis

For a discrete-time dynamic system, electric and thermal hysteresis analyses are carried out to explore the potential interference between two contiguous time steps before any control implementation. Extensive studies have shown that the voltage hysteresis phenomena do exist for lithium battery on account of thermodynamic entropic effects, mechanical stresses, and microscopic distortions [28,29]. For the equivalent circuit model illustrated in Fig. 1, when the current impulse terminates, only the RC circuit is still in effect with a time constant of  $\tau = R_D C_D$  and an initial potential of  $U_{ini} = IR_D$ . According to the investigation in Ref. [24], the calculated  $R_D$  and  $C_D$  are approximately 0.08 Ω and 0.4 F, respectively. Given the limited initial potential of the RC circuit, as long as the time step  $\delta t$  is much larger than the time constant  $\tau = 0.32$  s, it can be assumed that the discharge impulse has little impact on the next stage, and the electrical hysteresis can be neglected in this study.

With respect to thermal analysis, the main aim is to investigate the potential residual influence of the heat source to the temperature of next time step. The battery cell is treated as a flat plate along the flow direction, the relevant heat transfer efficiency of which can be evaluated by the Biot number that is defined as the ratio between the conductive resistance and the convective resistance, as given by:

$$Bi = \frac{hL_c}{k} \quad (5)$$

where  $h$  and  $k$  are the convective coefficient and conductive coefficient, respectively.  $L_c$  is the characteristic length, which is equal to half of the battery cell thickness. Based on similar experiment data extracted from Ref. [30],  $k$  and  $h$  are approximately equal to 7 W/(m K) and 20 W/(m<sup>2</sup> K) for low speed flow conditions, respectively. The calculated Biot number is much smaller than the evaluation criterion (0.1), implying that the conductive heat transfer capacity is much larger than that of convective heat transfer capacity. The internal temperature of the battery is uniformed, and the heat transfer can be simplified using a lumped thermal model, as expressed by:

$$mC_p \frac{\partial T}{\partial t} = -hA_s(T - T_\infty) + \dot{Q} \quad (6)$$

where  $m$ ,  $V$ , and  $A_s$  denote the mass, volume, and effective surface area of the battery, respectively.  $C_p$  is the average heat capacity,  $h$  represents the convective heat transfer coefficient, and  $T_\infty$  is the free stream temperature. It is observed that the identical battery temperature  $T$  is a function of time only, since the conductive resistance is negligible compared to the convective resistance. No thermal hysteresis is considered here based on the assumption.

## 2.3. CFD modeling of *J*-type BTMS

The *J*-type structure is originated from the widely used *U*- and *Z*-type configurations, as shown in Fig. 2. Theoretically, the two outlet valves are expected to be continuously adjusted and controlled according to the predefined optimal structure settings and battery operating conditions. However, the implementation of continuous control may unnecessarily consume excessive energy and require a more powerful real-time computational capacity as well. Consequently, it is reasonable to restrain the action interval or the change rate of the valve opening level. According to the parametric studies in Ref. [26], only three structures and their corresponding control modes are predefined in this paper for the sake of simplification, namely, *J*-mode, *Z*-mode, and *U*-mode, as presented in Fig. 2. The opening of the two valves under different working modes are represented by the configuration sizes of their corresponding outlets, as tabulated in Table 1. The time intervals between switching actions among the three modes are not predefined, which highly depends on the real-time condition.

The CFD modeling of the *J*-type BTMS is implemented using ANSYS Fluent with the  $k-\epsilon$  turbulence model, which has been validated with experiments in our previous study [26,31], as shown in Fig. 3. The battery cell is assumed to be homogeneous with a uniform internal heat source that is determined by the electro-thermal model and loaded using a user-defined function (UDF). Based on this CFD model, steady-state simulations and transient simulations are performed with different structural configurations in sequence. The main reason is that the time-independent steady-state simulation is used to optimize the *J*-type BTMS configurations with the best temperature distribution in steady cases; while the purpose of the time-dependent transient simulation is to establish a dynamic control plant model after the whole structure design is determined using structure optimization. Detailed settings of the CFD simulations can be found in our previous publication (Ref. [26]).

It is worth noting that the most conspicuous difference between the two simulations is the simulated time. For the steady state simulation,

**Table 1**  
Predefined control mode settings.

Control mode	Bottom inlet (mm)	Left outlet (mm)	Right outlet (mm)
<i>J</i> -mode	6	6	6
<i>U</i> -mode	6	8	4
<i>Z</i> -mode	6	4	8

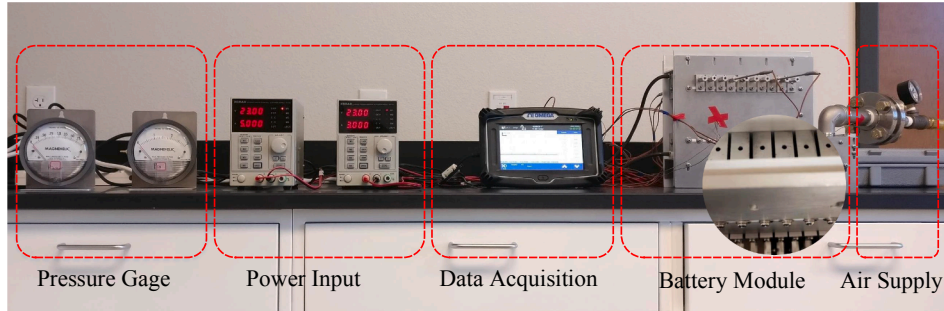


Fig. 3. Air-based BTMS experimental platform [26].

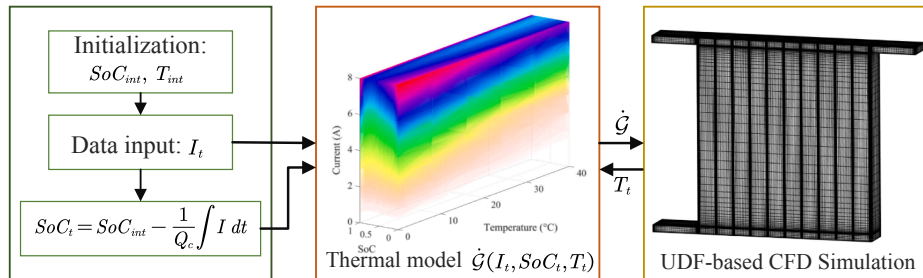


Fig. 4. The UDF framework of the transient flow CFD model.

the simulated time is not predefined as long as all the observed parameters approach to steady, whereas it is predefined by a time step  $\delta t$  in the transient simulation as demonstrated in Eq. (6). Fig. 4 shows the framework of the transient flow simulation, where the model inputs  $I_t$  and  $SoC_t$  stand for the Euclidean norm of current and the arithmetic average of  $SoC_t$  within a single time step, respectively; and  $T_t$  denotes the real-time battery temperature. In consequence, the response output of the transient simulation is the dynamic temperature augments of the battery cells labeled as 2, 4, 7, and 9 within a time step  $\delta t$ , namely,  $([T_{2t}, T_{4t}, T_{7t}, T_{9t}])$ . In this paper, the time step  $\delta t$  is set to be 5 s after comprehensive considerations of the computational cost, algorithm, and simulation accuracy. Each transient simulation takes approximately 45 min to converge on a six-core workstation. Note that the incoming cooling air temperature is only limited to 300 K, and scenarios with varying incoming temperatures are not yet considered in this study.

### 3. Neural network-based control system

The overall framework of the *J*-type BTMS thermal control system is presented in Fig. 5. The thermal control system consists of five major parts: a neural network-based (NN-based) controller, plant (battery system), external inputs (driving conditions), a mode switching module, and a reference temperature trajectory.

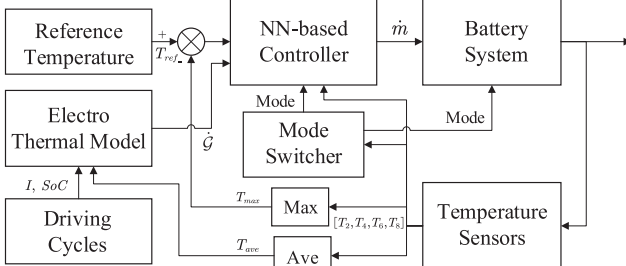
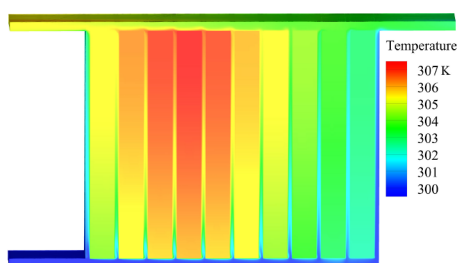
Prior to any control implementation, the *J*-type structure is optimized to provide more flexibility towards temperature control. With the

optimized structure, a large number of transient CFD simulations are conducted to build a data-driven plant model and controller as well. Here, the external input is referring to the tested driving cycle instead of the real-time drive conditions, which is derived as an equivalent heat source and regarded as one input to the controller.

#### 3.1. Structure pre-optimization for *J*-type BTMS

Previous studies have recognized that the BTMS structure, channel size in particular, has remarkable influences on the system's thermal performance [16]. For an air-based BTMS with parallel uniform-channel structure, there is actually a significant discrepancy in temperature distribution due to the uneven channel flow rate, as presented in Fig. 6. Generally, under severe battery operating conditions, e.g., a rapidly accelerating driving condition or a fast charging process, the cooling air mass flow rate is enhanced to constrain the battery temperature within a desirable range. However, it has very limited influence on the temperature uniformity, as shown in Fig. 7, especially under large mass flow rate conditions.

It is recognized that the temperature uniformity can not be improved effectively by simply increasing the air flow rate via control. Enhancing the uniformity via a structural pre-optimization before control is of great necessity. In this paper, surrogate-based optimization is employed to minimize the maximum temperature of the battery pack by rearranging the grouped channel sizes. As shown in Fig. 2, the channels of the battery pack are arranged into 5 groups (note 4 groups are used in our previous study [26]) as a trade-off between its optimal

Fig. 5. The thermal control framework of the *J*-type BTMS.Fig. 6. The CFD simulation of a *J*-type BTMS with even channels (3 mm).

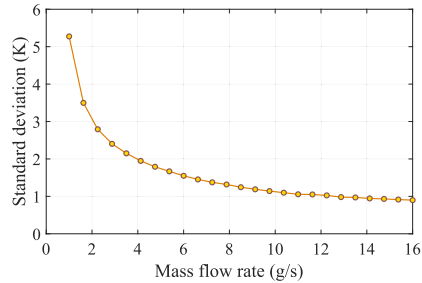


Fig. 7. The effects of the mass flow rate on the temperature uniformity.

thermal performance and the model accuracy. Another purpose is to design a *J*-type structure with an appropriate temperature distribution that enables flexible thermal control, e.g., the maximum temperatures should occur at the battery cells near the two outlets. The surrogate-based optimization problem is formulated as:

$$\begin{aligned} \arg \min_{X} \quad & T_{\max }=f\left(x_1, x_2, x_3, x_4, x_5\right) \\ \text { subject to } \quad & 2.0 \leqslant x_i \leqslant 3.5 \quad i=(1,2,3,4,5) \end{aligned} \quad (7)$$

where  $x_1-x_5$  represent the grouped channel sizes in millimeters. The algorithm and processing details of the ensemble surrogate-based optimization can be found in our previous study [26]. For the optimization and resampling process, the convergence criterion is defined as:

$$Bias=\left|\frac{Y_k^{*}-Y_{k-1}^{*}}{Y_{k-1}^{*}}\right| \leq 0.001 \quad (8)$$

where  $Y_k^*$  and  $Y_{k-1}^*$  are the best optimization result of the  $k$ -th resampling and the  $(k-1)$ -th resampling, respectively, and 0.001 is a pre-defined convergence tolerance.

The whole process terminates after two rounds of resampling, as shown in Fig. 8, and the resampled results converge to a small design range. The optimal results of the first and second rounds are 304.989 K and 304.954 K, respectively, and the normalized bias decreases to  $1.4E-10^4$ . The best sample among all the resampling data is treated as the optimal solution, as shown in Fig. 9. Compared with the case of even channels, it is seen that the maximum temperature has decreased from 307.18 K to 304.95 K, and the uniformity (represented by standard deviation) has significantly improved from 1.46 K to 0.42 K.

### 3.2. Battery temperature prediction model

In the primary stage concept design, the thermal control system prototype is implemented in the absence of an actual battery pack system since it is not readily available. A battery temperature prediction model is established here to represent the dynamic response of the battery system, which is also referred to as the plant model. Owing to the complexity and abusive assumptions of multi-channel parallel flow, it is impractical to estimate the dynamic temperature distribution using

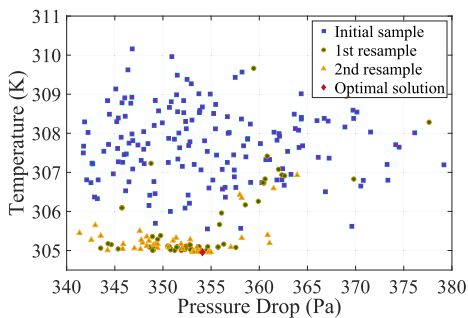


Fig. 8. The optimization and resampling process of the *J*-type BTMS with grouped channels.

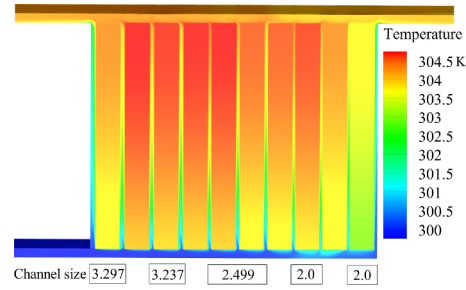


Fig. 9. The optimal solution and CFD simulation of the *J*-type BTMS with grouped channels.

an analytical solution. In this paper, a data-driven approach is adopted to implement the system identification, which reveals the multi-input multi-output (MIMO) relationship between the plant inputs (e.g., mass flow rate, initial temperature, and equivalent battery heat source) and the plant outputs (e.g., the updated temperatures of next time step), as defined by:

$$\left[T_{t+1}, T_{t+1}, T_{t+1}, T_{t+1}\right]=f\left(T_{\text {ave }}, \dot{m}, \dot{G}\right)+\left[T_{t}, T_{t}, T_{t}, T_{t}\right] \quad (9)$$

where  $T_{\text {ave }}$  is defined as the average of the initial battery temperature. Note that the equivalent heat source is calculated based on the initial electric characteristics and temperature in each time step.

As discussed in Section 2.3, three control modes are predefined for different scenarios. There are approximately 650 cases for each mode to be conducted with the transient flow CFD model based on the optimized BTMS structure. Sixty percent of the cases are generated using the Latin hypercube design of experiments algorithm, while the rest samples emphasize feasible design areas near the lower and upper bounds to increase the accuracy of sensitive regions.

Several typical stochastic black-box algorithms have been developed for the data-driven discrete time system identification, i.e., the auto-regressive moving average model, auto-regressive moving average with exogenous input, sparse identification of nonlinear dynamics with control, and neural network (NN) model [32,33]. Since all the raw samples are extracted from CFD simulations separately and randomly, the back propagation NN approach is employed here with the Levenberg–Marquardt training algorithm to establish the plant model. The hidden layers and neurons are determined by exhaustive searching after cross-validation, as tabulated in Table 2, where the multivariate normalized maximum absolute error (NMAE) and multivariate normalized root mean square error (NRMSE) are defined as:

$$N M A E_{m v}=\sum_{q=1}^m\left[\alpha_q\left(\frac{1}{n} \sum_{k=1}^n\left|\frac{\hat{y}_{q k}-y_{q k}}{y_{q \max }-y_{q \min }}\right|\right)\right] \quad (10)$$

$$N R M S E_{m v}=\sum_{q=1}^m\left[\beta_q \frac{1}{y_{q \max }-y_{q \min }} \sqrt{\frac{\sum_{k=1}^n\left(\hat{y}_{q k}-y_{q k}\right)^2}{n}}\right] \quad (11)$$

$$\sum_{q=1}^m \alpha_q=1 \quad \sum_{q=1}^m \beta_q=1 \quad (12)$$

where  $m$  and  $n$  stand for the sample dimension and sample size, respectively. The coefficient  $\alpha_q$  and  $\beta_q$  are assigned with an equal weight,

Table 2  
Plant model accuracy evaluation.

Mode	U-mode	Z-mode	J-mode
Layers & neurons	[5,4]	[7,5]	[4,4]
NMAE (%)	6.31	6.28	7.72
NRMSE (%)	5.95	5.86	7.37

$$\alpha_q = \beta_q = 0.25.$$

The mapping results are not as accurate as those of the surrogate models established for structure optimization in Ref. [26], in which the training data is based on steady-state simulation. The main reason is that transient simulations have a large number of cases that have a relatively small mass flow rate, in which the channel flow rate distribution largely differs from the benchmark case. Note that by adding more samples, the accuracy of the plant model could be potentially further improved. Given the highly nonlinear nature of fluid dynamics, the accuracy of the plant model via back propagation NN is reasonable and acceptable to be integrated into the thermal control system.

### 3.3. Neural network-based controller

For a CFD system, conventional control strategies like proportional-integral-derivative (PID) control may be not adequate to satisfy the control performance requirement. Advanced strategies like fuzzy logic control, adaptive neuro-fuzzy inference system, artificial neural network (ANN), NN-based adaptive PID control, and PID NN, have been successfully implemented in the literature [34]. Neural network is adopted here to construct and tune the controller using the same training data from transient simulations, in which the mass flow rate input is reversed as the output of the NN-based controller. The control goal is to generate an appropriate mass flow rate based on the temperature bias and operating mode, so as to closely follow the predefined temperature trajectory. Note that the actuator (e.g., cooling fan or compressor) is not considered here, since the output of the controller is same as the actuator. The relationships of the controller are expressed as:

$$\begin{aligned} \dot{m} &= g(T_{bias}, T_{ave}, \dot{\mathcal{G}}) \\ T_{bias} &= T_{ref} - \max(T_2, T_4, T_7, T_9) \\ T_{ave} &= (T_2 + T_4 + T_7 + T_9)/4 \end{aligned} \quad (13)$$

where the temperature bias is defined as the disparity between the reference temperature  $T_{ref}$  and the maximum temperature  $T_{max}$ , and the operating temperature is represented by the average temperature  $T_{ave}$ . The feasible range and change rate of the mass flow rate are constrained

by the actuator's actual operating limitations. Here, the constraints of the NN-based controller are predefined as:

$$\begin{aligned} 0 &\leq \dot{m} \leq 0.014 \\ |\Delta\dot{m}| &\leq 0.0035 \quad (\text{kg/s}) \end{aligned} \quad (14)$$

When the whole control system is put into practice, advanced adaptive self-tuning control algorithms, e.g., model identification adaptive control and model reference adaptive control, can be applied to adjust and improve both the plant model and the controller simultaneously by integrating the simulated results and real measured data.

### 3.4. Control mode switcher

As demonstrated in Fig. 2, the  $J$ -mode is designed for normal operation with higher efficiency, while the  $U$ -mode does bring in a stronger heat dissipation capacity to the left part, and the  $Z$ -mode acts similarly on the right part. By switching among the three modes, the temperature difference is expected to be fully constrained within a reasonable range. The switch logic for  $U$ - and  $Z$ -mode is defined as:

$$|T_{left} - T_{right}| = |\max(T_2, T_4) - \max(T_7, T_9)| \geq T_{uz} \quad (15)$$

where  $T_{left}$  and  $T_{right}$  refer to the maximum temperature of the left and right parts, respectively. The critical temperature for switching to  $U$ - and  $Z$ -mode is set as 0.5 K. When the left part has a higher temperature, the working mode will be switched to  $U$ -mode, and vice versa.

After three switches between the  $U$ - and  $Z$ -mode, the next action is to return back to the  $J$ -mode, and a switching cycle completes, as given by:

$$|T_{left} - T_{right}| \leq T_j \quad (16)$$

where the critical temperature switching to the  $J$ -mode ( $T_j$ ) is set to be 0.2 K. Each cycle traverses a  $J$ -,  $U$ -,  $Z$ -mode, and a half period of either  $U$ - or  $Z$ -mode in sequence, as illustrated in Algorithm 1. The duration of a switching cycle highly depends on the dynamic working conditions.

#### Algorithm 1. Control mode switching logic

```

Criterion U :  $T_{left} - T_{right} \geq T_{uz}$ 
Criterion Z :  $T_{right} - T_{left} \geq T_{uz}$ 
Criterion J :  $|T_{left} - T_{right}| \leq T_j$ 
Initialization: Mode= $J$ , Record=[ $J$ ]

while control process continues do
    if Criterion U & Mode  $\neq U$  then
        Record  $\Leftarrow$  [Record,  $U$ ]
        Mode  $\Leftarrow$   $U$ 
    end
    if Criterion Z & Mode  $\neq Z$  then
        Record  $\Leftarrow$  [Record,  $Z$ ]
        Mode  $\Leftarrow$   $Z$ 
    end
    if Record===[ $J, U, Z, U$ ]||[ $J, Z, U, Z$ ] & Criterion J then
        Record  $\Leftarrow$  [ $J$ ]
        Mode  $\Leftarrow$   $J$ 
    end
end

```

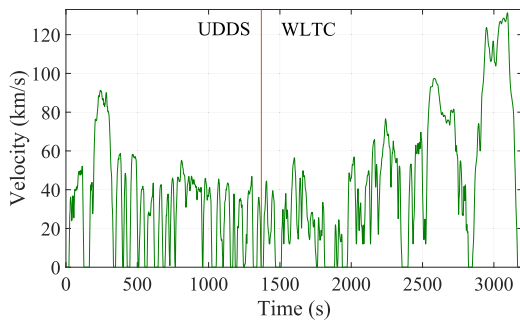


Fig. 10. The velocity profile of UDDS and WLTC.

**Table 3**  
EV specification and driving condition (TESLA Model 3).

Mass	m	1,875 kg	Road gradient	$\alpha$	0
Windward area	$A_f$	2.22 m <sup>2</sup>	Air friction Coeff	$C_d$	0.24
Standard gravity	$g$	9.8 m/s <sup>2</sup>	Motion efficiency	$\eta$	0.98
Air density	$\rho$	1.16 kg/m <sup>3</sup>	Rolling resistance	$\mu$	0.01
Velocity	$V$	–	Regenerative Coeff	$\eta_r$	0.8

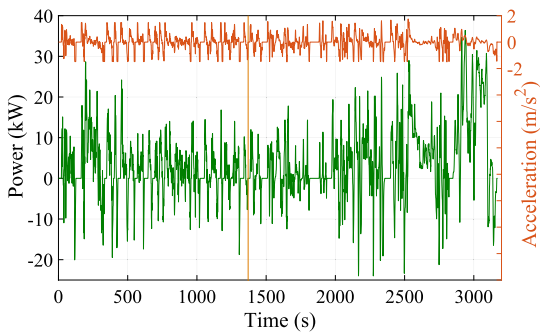


Fig. 11. The power and acceleration profiles of UDDS and WLTC.

### 3.5. Vehicle driving cycle and predefined temperature trajectory

During the control process, the driving cycle is considered as the dynamic input to the BTMS control system, while the predefined temperature trajectory serves as the reference for thermal control. For a running electric vehicle, the dynamic performance of the thermal system highly depends on the driving conditions that generally consists of several features, e.g., speed, acceleration velocity, SoC, and other operating conditions. Ideally, from the perspective of energy efficiency, BTMS as well as the battery management system should be adaptively controlled according to the real-time driving situations, which can also be predicted based on the driver's personal driving habits, vehicle stream, or transmitted directly from an autopilot system. For simplification, the EPA Urban Dynamometer Driving Schedule (UDDS) and the world-harmonized light-duty vehicles test cycle (WLTC) are directly utilized in this paper to test the dynamic response of the thermal management system, as illustrated in Fig. 10. The integrated driving cycle may repeat until the battery dies (SoC = 0). Note that this paper mainly focuses on the thermal response to dynamic driving conditions, except the driving power, other energy consumptions including the power for air conditioner, entertainments, and thermal control, are not considered in the current model.

Based on the velocity profile, the equivalent traction power is estimated using the power expression as below:

$$P = \frac{V}{1000\eta} [mg\cos\alpha + mgs\sin\alpha + \frac{1}{2}\rho A_f C_d V^2 + m\frac{dV}{dT}] \quad (17)$$

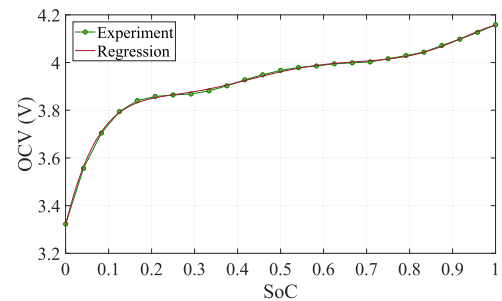


Fig. 12. The OCV-SoC correlation curve (Temperature: 315 K).

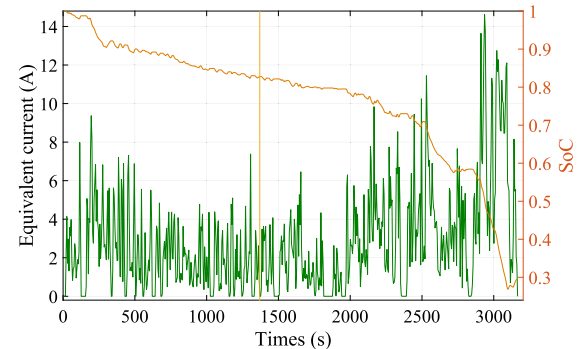


Fig. 13. The profiles of equivalent charging/discharging current and SoC.

Specific vehicle parameters and driving cycle conditions are tabulated in Table 3, where the vehicle is assumed to be running on a level road. Correspondingly, the power and acceleration profiles calculated based on the assumption are shown in Fig. 11, in which the negative power represents the portion that can be regenerated back into the battery system by a regenerative brake system with an efficiency of 0.8. The charging heat generation can also be estimated using the same electro-thermal model, since the reversible heat is significantly less than the resistance heat.

For the electrical settings of the vehicle, the EV's battery system consists of 6 battery modules in parallel, and every module has 110 battery cells in series. The battery has the same electric characteristics as the experiments conducted by Yang et al. [25], in which the battery nominal voltage and capacity are 3.75 V and 1.6 Ah, respectively. The specific open-circuit voltage (OCV)-SoC correlation curve developed in Ref. [24] is presented in Fig. 12. The temperature effect on the OCV-SoC relationship is neglected here for simplification. A polynomial regression model is adopted here to represent the relationship between OCV and SoC, given as: (see Fig. 13)

$$V_{oc} = -40.2SoC^6 + 138.6SoC^5 - 186.2SoC^4 + 123.5SoC^3 - 42.4SoC^2 + 7.5SoC^1 + 3.32 \quad (18)$$

Based on the battery model proposed by Zhao et al. [35], the equivalent current and corresponding SoC are calculated using the equation  $P = V_i I$  with a temporal resolution of 1 s. To be consistent with the transient simulations, the time step is extended to 5 s ( $\delta t = 5$  s) for simulation and control convenience. In addition, according to the thermal expression derived in Eq. (2), the quadratic mean of current and the arithmetic mean of SoC are derived to represent the initial electric characteristics for simulations, given as:

$$I = \sqrt{\frac{1}{n} \sum_{i=1}^n I_i^2} \quad SoC = \frac{1}{n} \sum_{i=1}^n SoC_i \quad n = 5 \quad (19)$$

Considering the real-time operating temperature, the equivalent heat source is derived and treated as the external input to the system.

Ideally, the reference temperature trajectory should also ideally be

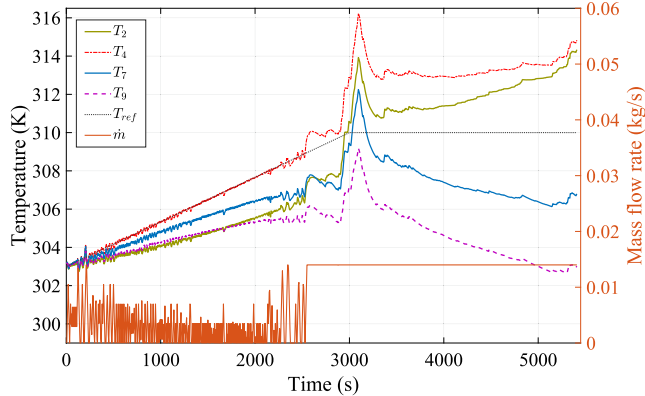


**Fig. 14.** The battery temperatures and mass flow rate using the NN-based thermal control without mode switching.

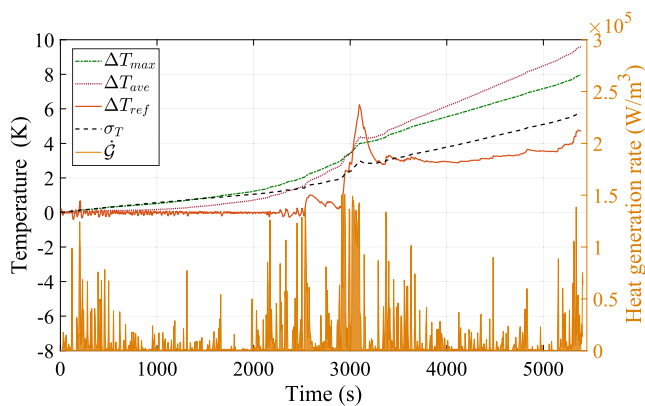


**Fig. 15.** Temperature uniformity and equivalent heat source ( $\Delta T_{max}$  is the temperature difference between the maximum temperature of the left part and the right part, which is also the control temperature for mode switching.  $\Delta T_{ave}$  is the difference between the average temperature of the left part and the right part.  $\Delta T_{ref}$  is the difference between the maximum temperature of the battery pack and the reference temperature.  $\sigma_T$  is the temperature standard deviation of the battery pack.).

determined and adjusted adaptively according to the real-time driving conditions, e.g., strenuous driving requires an aggressive temperature augment trajectory, while a gradual rise temperature curve is sufficient enough for smooth driving. In this paper, considering the driving cycles illustrated above, the reference temperature trajectory consists of a climbing section from 303 K to 310 K in 50 min and a stable section of 310 K. The maximum temperature is expected to be fully restrained within 313.15 K with a reference temperature of 310 K.

#### 4. Case study

##### 4.1. Neural network-based control without mode switching

The basic control strategy without the predefined mode switching module is conducted as a benchmark. As seen in Fig. 5, the mode switching module is bypassed, and thus the battery system only operates in *J*-mode. By applying the comprehensive driving test cycle in Fig. 10, the dynamic temperature distributions and mass flow rate are obtained, as shown in Fig. 14. It is observed that the maximum temperature of the battery pack is able to follow the reference temperature by controlling and adjusting the mass flow rate. However, the trend of temperature deviation starts in approximately 2,500 s due to the accumulation of a large amount of heat, though the mass flow rate has already been controlled and increased to its upper bound, as presented in Fig. 15.

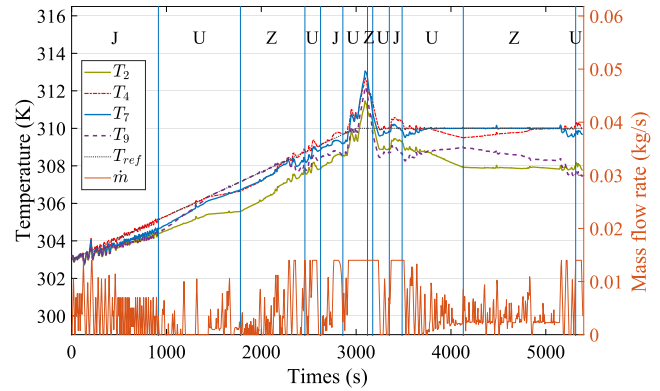


**Fig. 16.** The battery temperatures and mass flow rate using the NN-based thermal control with mode switching.

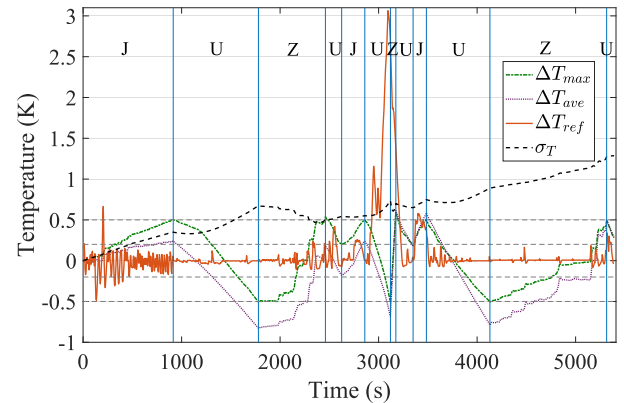


**Fig. 17.** The mode switching details and battery temperature uniformity of the NN-based control.

Another evaluation criterion, the temperature uniformity characterized by the temperature standard deviation, also deteriorates in the meantime, as shown in Fig. 15. It should be noted that the *J*-type structure is optimized under the setting of approximately 52% full mass flow rate. Under the full mass flow rate condition, the cooling effects are more significant on the right part of the battery pack, making the heat dissipation of the 7th and 9th cells much stronger as shown in Fig. 14, due to the distinct nature of the optimized *J*-type structure. Once the external heat source drops off, it is foreseeable that the maximum temperature will be restored back to the reference temperature, while the lower temperature will be kept at the current level.

It is seen from Fig. 14 that the maximum battery pack temperature difference under the NN-based control without mode switching is 11 K, due to the temperature deviations accumulated during the dynamic process. Our previous study has already shown the distinguished advantages of the *J*-type structure in terms of temperature uniformity compared to the traditional *U*- and *Z*-type structures [26]. Thus the dynamic thermal performance will be even worse for traditional structures, i.e., *U*-type and *Z*-type. There is scarcely any solution to address this issue but to increase the mass flow. Instead of increasing the capacity of mass flow rate, we will explore if the mode switching technique can further improve the performance of BTMS in this study.

##### 4.2. Neural network-based control with mode switching

Considering the mode switching module in the control framework as shown in Fig. 5, the corresponding responses regarding the temperature and mass flow rate are calculated, as shown in Fig. 16. Compared to the results without mode switching in Fig. 14, it is seen that the temperature difference between  $T_2$  and  $T_9$  exceeds the switching

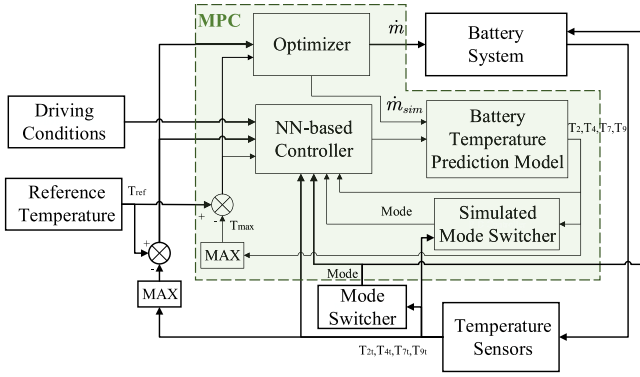


Fig. 18. The overall framework of the NN-based MPC strategy.

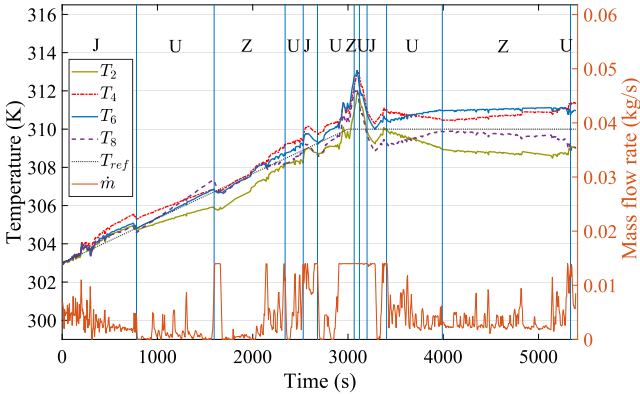


Fig. 19. The battery temperatures and mass flow rate with the NN-based MPC strategy.

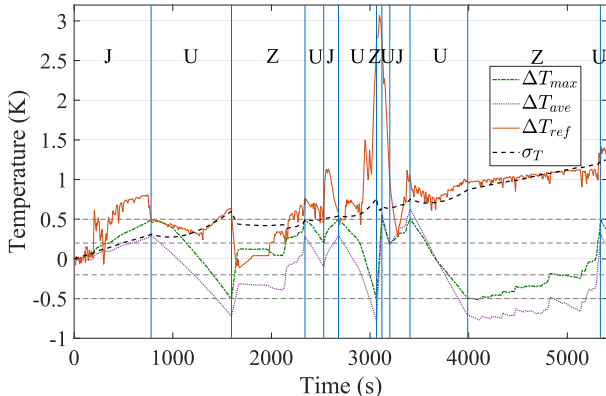


Fig. 20. The mode switching details and battery temperature uniformity of the NN-based MPC strategy.

threshold 0.5 K at around 900 s, the temperature difference stops increasing by switching the operation mode from *J*-mode to *U*-mode, and followed by mode switching from *U*-mode to *Z*-mode, and continues. The battery temperatures closely follow the reference trajectory during

the entire process, except under the intense driving conditions at around 3,000 s, where the battery temperature slightly exceeds the predefined ceiling temperature.

The temperature uniformity under the NN-based control with mode switching is also significantly better than that of the control without mode switching, as shown in Fig. 17. In addition, Fig. 17 also shows the tendency of the temperature difference between the left part and the right part during the entire transition process. Overall, we find that the NN-based control with mode switching is able to control the maximum temperature and balance the temperature uniformity simultaneously.

#### 4.3. Neural network-based model predictive control

As shown in Fig. 16, there exist very rapid changes to the mass flow rate, while the battery temperatures are well controlled according to the reference temperature. This is mainly due to that the NN-based control strategy only considers the temperature bias of the last step and the external input at the current step, and does not foresee the possible approaching drastic changes in the external input. To further improve the control performance, an MPC approach is employed here and integrated with the NN-based control system.

The overall control framework is illustrated in Fig. 18, where the MPC module is added to forecast and optimize the controller output. The main objective of MPC is to minimize the cost function as follows:

$$\begin{aligned} \arg \min_m J = & \sum_{k=n}^{n+N} (\alpha_k \sum_{b=2}^{[2,4,7,9]} (T_{ref_k} - T_{bk})^2) + \sum_{k=n}^{n+N-1} \beta_k (\dot{m}_{k+1} - \dot{m}_k)^2 \\ \text{subject to } & 0 \leq \dot{m} \leq 0.014 \\ & |\Delta \dot{m}| \leq 0.0035 \end{aligned} \quad (20)$$

where  $n$  is the current control step, and  $N$  is the control horizon, here,  $N = 4$ . The parameter  $\alpha_k$  is a weight factor that reflects the relative importance of the temperature difference, while the coefficient  $\beta_k$  penalizes the relatively big changes in the mass flow rate. By adjusting the two coefficients, different control strategies can be achieved for different purposes.

Owing to the high nonlinearity of the control problem, the genetic algorithm (GA) optimizer is adopted here to solve the optimization problem by considering several steps ahead. It should be noted that GA does not have high computational efficiency. For optimal control, to better balance the performance and computational efficiency, a local optimum (or a better solution) is acceptable here as long as the performance is improved. The optimization convergence criteria can be adjusted and tuned based on the time requirement and accuracy settings.

Fig. 19 shows the battery temperatures and mass flow rate with the NN-based MPC strategy. While the battery temperatures well follow the reference temperature at most of the time, there still exist deviations at several time periods, e.g., 400–1,000 s, 2,000–2,400 s, and after 3,200 s. The main reason is that the penalization term (i.e., the second term in Eq. (20)) dominates the cost function. Whenever the penalty cost of increasing the mass flow rate prevails over that of the temperature deviation, the MPC strategy tends to reduce the variability of the mass flow rate, so as to improve the smoothness of the thermal control system as well as the energy efficiency. Similarly, the temperature changes during the mode switching process and temperature uniformity are presented in Fig. 20. It is seen that the temperature

Table 4  
Summaries of the three control strategies.

Control strategy	Maximum temperature (K)	Temperature uniformity (K)	Energy (J)
Control without mode switching	316.10	5.81	51,384
Control with mode switching	313.17	1.33	17,412
MPC with mode switching	313.12	1.25	14,678

uniformity is 7.4% better than that without MPC, though the temperatures deviate from the reference trajectory.

#### 4.4. Energy efficiency analysis

For simplification, it is assumed that the cooling air is provided by an axial flow fan, and the energy consumption of BTMS can be calculated by:

$$N_p = \int_0^n \frac{\dot{m} \Delta P}{\rho \eta} dt \quad (21)$$

where  $\Delta P$  is the pressure augment of the fan,  $\rho$  is the air density, and  $\eta$  is the overall efficiency ( $\eta = 0.75$ ).

The pressure augment relates to the mass flow rate, which can also be obtained via transient flow simulations. In this study, a support vector regression model is established to represent the pressure augment as a function of the mass flow rate. The energy consumption, as well as the maximum temperature and the temperature uniformity, is tabulated in Table 4. It is observed that the NN-based control without mode switching fails to meet the thermal requirements in terms of the maximum temperature and temperature uniformity. In addition, by employing MPC, the energy efficiency has an approximately 15.8% improvement compared to NN-based with mode switching, with a cost of slight deviation from the reference temperature. Given the critical operation temperature is 313.15 K, it is reasonable to employ the MPC strategy with a reference temperature of 310 K.

## 5. Conclusion

This paper developed a self-adaptive intelligent air-based *J*-type battery thermal management system via neural network-based model predictive control. Prior to any control implementation, surrogate-based *J*-type structure optimization was first performed to improve the temperature uniformity and enhance the control flexibility using steady-state CFD simulations.

Based on the optimized structure and the established electro-thermal-fluid model, a large number of transient fluid dynamics simulations were conducted for the three predefined operation modes (i.e., *J*-, *Z*-, and *U*-mode) to build control models using the neural network algorithm. By applying dynamic driving cycles, the impacts of mode switching was investigated in the case study. Results showed that the NN-based control without mode switching failed to control the thermal system in terms of both the maximum temperature and temperature uniformity, while the NN-based control with mode switching was able to regulate the maximum temperature within the critical safety temperature and balance the temperature uniformity within 1.5 K under varying working conditions. It was also found that there was a 15.8% energy efficiency improvement by employing model predictive control.

It was verified that the developed self-adaptive BTMS control strategy was able to meet the thermal requirements for battery system. However, the model predictive control in this study emphasized more on the energy efficiency rather than the maximum temperature control. Note that this study has not yet considered the thermal impacts from other factors such as the air conditioner energy consumption and the potential overlapped power peaks. Potential future work will (i) study the two coefficients in model predictive control to develop a balanced control strategy, and (ii) investigate and determine when to employ MPC for the thermal system.

## Declaration of Competing Interest

The authors declare that they have no known competing financial interests or personal relationships that could have appeared to influence the work reported in this paper.

## References

- [1] Lu L, Han X, Li J, Hua J, Ouyang M. A review on the key issues for lithium-ion battery management in electric vehicles. *J Power Sources* 2013;226:272–88.
- [2] Hannan MA, Lipu MH, Hussain A, Mohamed A. A review of lithium-ion battery state of charge estimation and management system in electric vehicle applications: challenges and recommendations. *Renew Sustain Energy Rev* 2017;78:834–54.
- [3] Pesaran A, Santhanagopalan S, Kim G. Addressing the impact of temperature extremes on large format li-ion batteries for vehicle applications (presentation). Tech. rep., National Renewable Energy Lab. (NREL), Golden, CO (United States); 2013.
- [4] Park C, Jaura AK. Dynamir thermal model of li-ion battery for predictive behavior in hybrid and fuel cell vehicles. Tech rep, SAE Technical Paper; 2003.
- [5] Xia G, Cao L, Bi G. A review on battery thermal management in electric vehicle application. *J Power Sources* 2017;367:90–105.
- [6] Grande L, He X. Advanced li-ion beyond li-ion batteries 2018–2028, [Online] Available at: <<https://www.idtechex.com/research/reports/advanced-li-ion-and-beyond-li-ion-batteries-2018-2028-000566.asp>>, [accessed Jan 2018].
- [7] Jaguemont J, Boulon L, Dubé Y. A comprehensive review of lithium-ion batteries used in hybrid and electric vehicles at cold temperatures. *Appl Energy* 2016;164:99–114.
- [8] Wang X, Li M, Liu Y, Sun W, Song X, Zhang J. Surrogate based multidisciplinary design optimization of lithium-ion battery thermal management system in electric vehicles. *Struct Multidiscip Optim* 2017;56(6):1555–70.
- [9] Xun J, Liu R, Jiao K. Numerical and analytical modeling of lithium ion battery thermal behaviors with different cooling designs. *J Power Sources* 2013;233:47–61.
- [10] Park H. A design of air flow configuration for cooling lithium ion battery in hybrid electric vehicles. *J Power Sources* 2013;239:30–6.
- [11] He F, Ma L. Thermal management of batteries employing active temperature control and reciprocating cooling flow. *Int J Heat Mass Transf* 2015;83:164–72.
- [12] Yang N, Zhang X, Li G, Hua D. Assessment of the forced air-cooling performance for cylindrical lithium-ion battery packs: a comparative analysis between aligned and staggered cell arrangements. *Appl Therm Eng* 2015;80:55–65.
- [13] Shahid S, Agelin-Chaab M. Analysis of cooling effectiveness and temperature uniformity in a battery pack for cylindrical batteries. *Energies* 2017;10(8):1157.
- [14] Wang T, Tseng K, Zhao J, Wei Z. Thermal investigation of lithium-ion battery module with different cell arrangement structures and forced air-cooling strategies. *Appl Energy* 2014;134:229–38.
- [15] Saw LH, Poon HM, San Thiam H, Cai Z, Chong WT, Pambudi NA, et al. Novel thermal management system using mist cooling for lithium-ion battery packs. *Appl Energy* 2018;223:146–58.
- [16] Kim J, Oh J, Lee H, Review on battery thermal management system for electric vehicles. *Appl Therm Eng*.
- [17] Gao X, Ma Y, Chen H. Active thermal control of a battery pack under elevated temperatures. *IFAC-PapersOnLine* 2018;51(31):262–7.
- [18] Masoudi Y, Azad NL. Mpc-based battery thermal management controller for plug-in hybrid electric vehicles. In: 2017 American control conference (ACC), IEEE; 2017. p. 4365–70.
- [19] Wang H, He F, Ma L. Experimental and modeling study of controller-based thermal management of battery modules under dynamic loads. *Int J Heat Mass Transf* 2016;103:154–64.
- [20] Tao X, Wagner J. A thermal management system for the battery pack of a hybrid electric vehicle: modeling and control. *Proc Inst Mech Eng, Part D: J Automob Eng* 2016;230(2):190–201.
- [21] Vatanparvar K, Al Faruque MA. Otem: optimized thermal and energy management for hybrid electrical energy storage in electric vehicles. In: 2016 Design, automation & test in Europe Conference & Exhibition (DATE), IEEE; 2016. p. 19–24.
- [22] Liu Y, Ghassemi P, Chowdhury S, Zhang J. Surrogate based multi-objective optimization of j-type battery thermal management system. In: ASME 2018 International design engineering technical conferences and computers and information in engineering conference, American Society of Mechanical Engineers; 2018. p. V02BT03A034–V02BT03A034.
- [23] Cheng X-B, Zhang R, Zhao C-Z, Zhang Q. Toward safe lithium metal anode in rechargeable batteries: a review. *Chem Rev* 2017;117(15):10403–73.
- [24] Yang Z, Patil D, Fahimi B. Online estimation of capacity fade and power fade of lithium-ion batteries based on input-output response technique. *IEEE Trans Transport Electr* 2018;4(1):147–56.
- [25] Yang Z, Patil D, Fahimi B. Electrothermal modeling of lithium-ion batteries for electric vehicles. *IEEE Trans Veh Technol* 2019;68(1):170–9.
- [26] Liu Y, Zhang J. Design a j-type air-based battery thermal management system through surrogate-based optimization. *Appl Energy* 2019;252:113426.
- [27] Dai H, Wei X, Sun Z, Wang J, Gu W. Online cell soc estimation of li-ion battery packs using a dual time-scale kalman filtering for ev applications. *Appl Energy* 2012;95:227–37.
- [28] Dong G, Wei J, Zhang C, Chen Z. Online state of charge estimation and open circuit voltage hysteresis modeling of LiFePO<sub>4</sub> battery using invariant imbedding method. *Appl Energy* 2016;162:163–71.
- [29] Marongiu A, Nußbaum FGW, Waag W, Garmendia M, Sauer DU. Comprehensive study of the influence of aging on the hysteresis behavior of a lithium iron phosphate cathode-based lithium ion battery—an experimental investigation of the hysteresis. *Appl Energy* 2016;171:629–45.
- [30] Ling Z, Wang F, Fang X, Gao X, Zhang Z. A hybrid thermal management system for lithium ion batteries combining phase change materials with forced-air cooling. *Appl Energy* 2015;148:403–9.
- [31] Liu Y, Li M, Zhang J. An experimental parametric study of air-based battery thermal management system for electric vehicles. In: ASME 2017 International design

- engineering technical conferences and computers and information in engineering conference, American Society of Mechanical Engineers; 2017. p. V02AT03A024–V02AT03A024.
- [32] Saxén H, Gao C, Gao Z. Data-driven time discrete models for dynamic prediction of the hot metal silicon content in the blast furnace—a review. *IEEE Trans Industr Inform* 2012;9(4):2213–25.
- [33] Brunton SL, Proctor JL, Kutz JN. Discovering governing equations from data by sparse identification of nonlinear dynamical systems. *Proc Nat Acad Sci* 2016;113(15):3932–7.
- [34] Afram A, Janabi-Sharifi F. Theory and applications of hvac control systems—a review of model predictive control (mpc). *Build Environ* 2014;72:343–55.
- [35] Zhao X, de Callafon RA. Modeling of battery dynamics and hysteresis for power delivery prediction and soc estimation. *Appl Energy* 2016;180:823–33.